Grating Optimization for Smith–Purcell Radiation: Direct Correlation Between Spatial Growth Rate and Starting Current

Md Arifuzzaman Faisal, and Peng Zhang, *Senior Member, IEEE*

***Abstract*— Smith–Purcell radiation (SPR) is generated when electrons travel close to a metallic periodic grating. It was found that the starting current of SPR varies by orders of magnitude by simply varying the grating parameters (groove's heights and widths) while keeping the grating period and the electron beam properties fixed. In this article, we demonstrate that this strong dependence of starting current on the grating parameters is directly related to the spatial growth rate of the SPR. Using the hot-tube dispersion relation, we optimize the grating parameters to minimize the starting current to excite coherent SPR.**

***Index Terms*— Grating optimization, growth rate, hot-tube dispersion relation, Smith–Purcell radiation (SPR), starting current.**

I. Introduction

HIGH-POWER, efficient, and low-cost electromagnetic sources have significant uses in high-resolution imaging, biomedical scanning, material analysis, security systems, high-data-rate communications, and so on. As a special case of backward wave oscillator (BWO), Smith–Purcell radiation (SPR) has attracted strong interest in producing terahertz (THz) radiation. When an electron beam travels with a velocity v above a metallic periodic grating of period L, SPR can be generated with wavelength λ at an angle θ. (see Fig. 1), described by [1]

$$\lambda = \frac{L}{n}\left(\frac{1}{\beta} - \cos\theta\right) \tag{1}$$

where n is an integer, $\beta = v/c$, and c is the speed of light.

As an Orotron-like device proposed by Rusin and Bogomolov [2], SPR operation depends on the grating parameters, though not reflected in (1). Rusin also investigated the possibilities to decrease starting current by grating modification more than 50 years ago. The dependence of starting current on grating parameters for SPR is analyzed in previous studies [3], [4], [5], [6], which typically calculate the growth rate in time (i.e., imaginary component of frequency) and rely on the boundary conditions at the ends of the interacting structure.

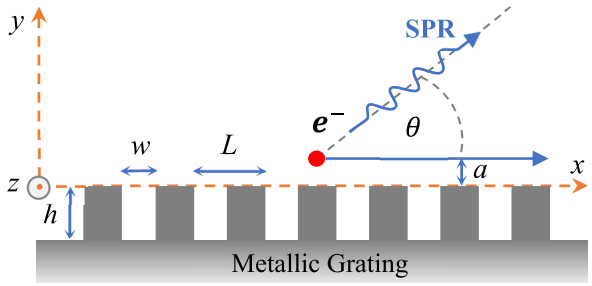

Fig. 1. Schematic of Smith–Purcell grating and beam configuration.

In this article, we systematically study the cold- and hot-tube dispersion relations for THz SPR at different grating parameters (groove's heights and widths) with a fixed grating period. The change of the SPR operating points with different grating parameters is obtained from the cold-tube dispersion relation. We then solve the hot-tube dispersion relation to find the spatial growth rate (i.e., imaginary component of wavenumber), which is compared with the starting current calculated from particle-in-cell (PIC) simulations [3]. Strong correlation between the starting current and spatial growth rate is demonstrated, without considering the boundary conditions at the ends of the interaction structures. In contrast to previous studies based on the time growth rate and on the end boundary conditions of the grating, our simple approach by only calculating the spatial growth rate based on the hot-tube dispersion relation can be used to determine the optimal grating parameters for minimization of the starting current efficiently.

II. Cold-Tube Dispersion Relation

The cold-tube dispersion for the SPR model in Fig. 1 is [3]

$$\frac{\cot(\bar{\omega}\bar{H})}{\bar{\omega}\bar{H}} - \sum_{n=-\infty}^{\infty}\left(\frac{\sin\theta_n}{\theta_n}\right)^2\frac{\bar{W}}{\gamma_n\bar{H}} = 0 \tag{2}$$

where the normalized grating groove width $\bar{W} = w/L$, grating height $\bar{H} = h/L$, frequency $\bar{\omega} = \omega L/c$, wavenumber $\bar{k} = kL$, $\theta_n = P_n\bar{W}/2$, $\gamma_n = (P_n^2 - \bar{\omega}^2)^{1/2}$, $P_n = \bar{k} + 2n\pi$, L is the grating period, and n is an integer. Equation (2) is for the evanescent (surface mode) wave that is derived by assuming transverse electromagnetic (TEM) mode inside the grooves, which is matched to the Floquet fields outside the grating [3], [7], [8]. Note that, while the strict solution of

Manuscript received 6 August 2022; revised 16 September 2022; accepted 20 September 2022. Date of publication 10 October 2022; date of current version 25 May 2023. This work was supported by the Air Force Office of Scientific Research (AFOSR) YIP Grant FA9550-18-1-0061, the Office of Naval Research (ONR) YIP Grant N00014-20-1-2681, and the Air Force Office of Scientific Research (AFOSR) Grant FA9550-20-1-0409. The review of this article was arranged by Editor Y. Gong. *(Corresponding author: Peng Zhang.)*

The authors are with the Department of Electrical and Computer Engineering, Michigan State University, East Lansing, MI 48824 USA (e-mail: pz@egr.msu.edu).

Color versions of one or more figures in this article are available at https://doi.org/10.1109/TED.2022.3208846.

Digital Object Identifier 10.1109/TED.2022.3208846

TABLE I
MAIN PARAMETERS FOR THE CALCULATION

Beam energy	50 keV
Beam Height from Grating Surface, a	10 μm
Beam thickness, τ	10 μm
Beam Current, I	5000 A/m
Grating period, L	120 μm

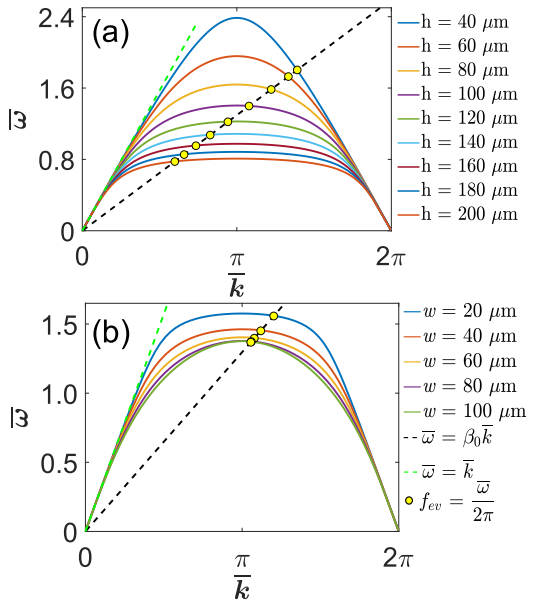

Fig. 2. Cold-tube dispersion relation [see (2)] for (a) different groove's height h where groove's width w is fixed at 60 μm, (b) different w where h is fixed at 100 μm, and other parameters are kept as the same as in Table I. The yellow dots denote the operation points at the evanescent wave frequency f_{ev}.

cold- (and hot-) tube dispersion relation for BWO is general and mature, including higher order modes [4], [5], [6], [9], [10], [11], here, for simplicity, we consider only TEM mode in the grooves in the dispersion, as SPR is primarily caused by TEM modes there [12], [13], [14], [15], [16], [17], [18], and such dispersion calculation is found in excellent agreement with full-wave PIC simulations [3]. In the numerical calculation of (2) as well as (3) later, we used a maximum of $n = 50$ to ensure convergence.

Fig. 2 shows the cold-tube SPR dispersion curves at different grating groove's heights and widths, with all the other parameters as in Table I, which follows [3]. The operating frequency of the evanescent surface mode f_{ev} is determined by the intersection of the beamline $\bar{\omega} = \beta_0 \bar{k}$ with the dispersion relation [see (2)], as shown in Fig. 2, for the beam velocity to light speed radio $\beta_0 = 0.4126$ for a 50-keV beam. SPR radiation occurs at the corresponding second harmonic of this frequency, $2f_{ev}$.

It is clear that with fixed beam energy and grating period, f_{ev} varies significantly with the change of grating groove's width and height [3], [4], whereas (1) only shows that SPR varies with the change of grating period for fixed beam energy. Note that the decrease of operation frequency with the increase of the groove's height h is consistent with that of slow wave structure at gigahertz frequency [19, Fig. 15]. While for most of the cases, the slope (or the group velocity) $d\bar{\omega}/d\bar{k}$ of the dispersion curve at the oscillating point

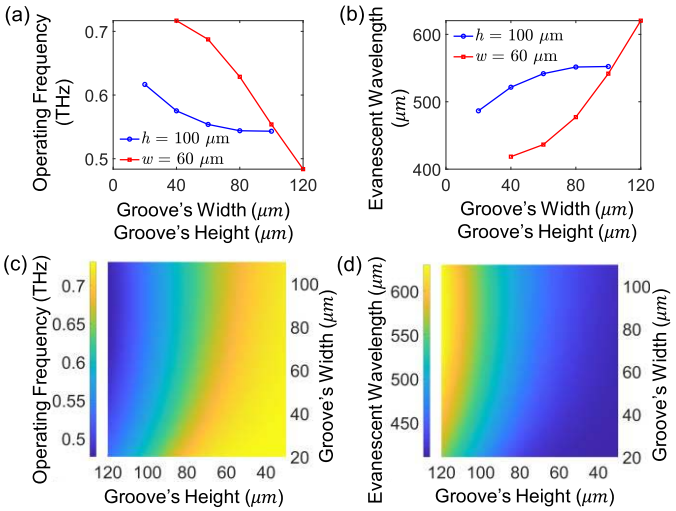

Fig. 3. (a) Operating frequency (f_{ev}) and (b) corresponding evanescent wavelength (λ_{ev}) as a function of grating groove's height and width, with red line for Fig. 2(a) and blue line for Fig. 2(b) [3]. The surface plot of (c) f_{ev} and (d) λ_{ev} for a wide range of groove's heights and widths, with other parameters in Table I.

is negative, it is interesting to note that for the cases of $h = 120$–200 μm in Fig. 2(a), the group velocity becomes positive, indicating that simply varying grating parameters can modify the beam–grating interaction from backward wave to forward wave operation.

The operation frequency f_{ev} and the corresponding wavelength $\lambda_{ev}(= c/f_{ev})$ in Fig. 2 are plotted in Fig. 3(a) and (b), respectively [3]. As either w or h increases, f_{ev} (λ_{ev}) decreases (increases), which can be explained by the more rounded and lowered band edge in Fig. 2, resulting in an intersection point at a smaller frequency with fixed beam energy. This general trend of f_{ev} and λ_{ev} on w and h is also confirmed for a wide range of parameters in Fig. 3(c) and (d).

III. HOT-TUBE DISPERSION AND GROWTH RATE

The hot-tube dispersion is derived using a similar field theory approach as for the cold-tube dispersion, with the inclusion of a continuous electron beam, by solving Maxwell's equations coupled with beam continuity equation and the equation of motion consistently [8]. The hot-tube dispersion for the SPR in Fig. 1 is

$$f(\bar{k},\bar{\omega}) \equiv \frac{\cot(\bar{\omega}\bar{H})}{\bar{\omega}\bar{H}} - \sum_{n=-\infty}^{\infty} U_n \left(\frac{\sin\theta_n}{\theta_n}\right)^2 \frac{\bar{W}}{\gamma_n \bar{H}} = 0$$
$$\text{with} \quad U_n = \frac{1 - \Psi\cosh(\gamma_n \overline{A})/e^{\gamma_n \overline{A}}}{1 - \Psi\sinh(\gamma_n \overline{A})/e^{\gamma_n \overline{A}}} \tag{3}$$

where the normalized beam distance from the grating $\bar{A} = a/L$, $\Psi = \bar{\omega_a}^2\gamma_n/(\overline{\omega} - p_n\beta_0)^2$, $\bar{\omega_a} = \omega_a L^{1/2}/c$, $\omega_a^2 = (e^2 n_0/m\epsilon_0)\tau = \omega_p^2\tau$, ω_p is the plasma frequency, n_0 is the number of electrons per unit volume, τ is the thickness of beam, $\beta_0 = v_0/c$, v_0 is the beam velocity, and all the other symbols are defined as in (2). As seen in (3), the beam–grating distance a needs to be kept small in order to achieve strong interaction. The effect of beam alignment (and misalignment) would be the subject of future research.

The hot-tube dispersion relation [see (3)] is solved to obtain the complex wavenumber $\overline{k} = \bar{k}_r + j\bar{k}_i$ for a given operating frequency $\overline{\omega}$. With $\sim e^{-j\omega t + jkx}$ dependence for the fields when

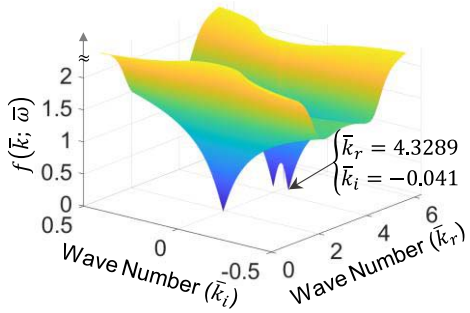

Fig. 4. Roots of (3) where the grating parameters are $w = 60$ μm and $h = 40$ μm and the corresponding operating frequency $\overline{\omega} = 1.80444$ [cf. Fig. 2(a)].

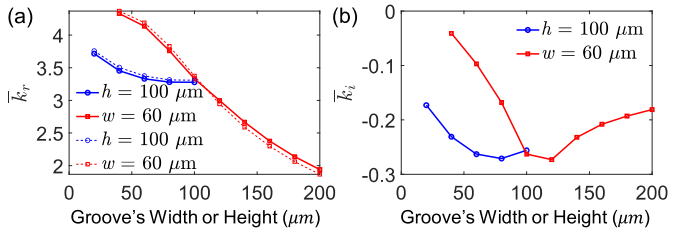

Fig. 5. (a) Real and (b) imaginary parts of the wavenumber at the operating frequency $\overline{\omega} = 2\pi f_{ev} L/c$ determined from (2), as a function of the groove height h (squares, groove width w fixed at 60 μm) as well as groove width w (rounds, h fixed at 100 μm), calculated from the hot dispersion relation (3). Dashed lines in (a) are for the wavenumber at f_{ev} calculated from the cold-tube dispersion (2). The other parameters are kept the same as in Table I.

deriving (3), a negative imaginary part of the wavenumber $k = k_r + jk_i$ indicates a growing wave as a function of position as $e^{-k_i x}$, with $-k_i$ being the growth rate. For the grating parameters $w = 60$ μm and $h = 40$ μm and the corresponding operating frequency $\overline{\omega} = 1.80444$ [from Fig. 2(a)], the roots are calculated from (3) by setting $f(\bar{k}, \bar{\omega}) = 0$, as shown in Fig. 4. We will consider only the root where the imaginary part of the wavenumber is negative, which gives $\bar{k}_r = 4.3289$ and $\bar{k}_i = -0.041$.

Fig. 5 plots the real and imaginary parts of the complex wavenumber $\overline{k} = \bar{k}_r + j\bar{k}_i$ with a negative $\bar{k}_i$ at the operating frequency $\overline{\omega}(= 2\pi f_{ev})$ determined by the cold-tube dispersion in Fig. 2, as a function of the groove height h (width w is kept at 60 μm) and groove width w (h is kept at 100 μm), while the rest of the parameters remain the same as those in Table I.

Compared to the wavenumber at f_{ev} at the intersection point of the beam mode and the cold-tube dispersion curve in Fig. 2 [dashed line in Fig. 5(a)], $\bar{k}_r$ [solid line in Fig. 5(a)] calculated from the hot-tube dispersion is slightly shifted, due to the detuning effect of the electron beam [20], [21], [22].

Just as the real part, $\bar{k}_i$ also depends strongly on the grating parameters. As shown in Fig. 5(b), there is a maximum spatial growth rate $-\bar{k}_i$ around $h = 100$ and 120 μm for fixed w and around $w = 80$ μm for fixed h. It is important to note that these maximum growth rates occur when the corresponding operating points become closest to the upper band edge of the cold-tube dispersion curve in Fig. 2, where the band edge is known to be susceptible to instabilities to trigger oscillation [23].

IV. Starting Current of SPR

When a continuous electron beam passes over grating, its interaction with the grating structure would induce velocity

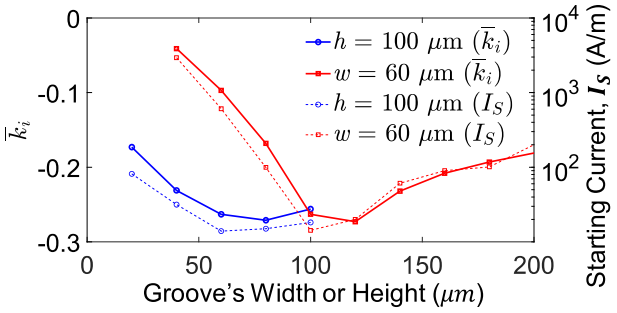

Fig. 6. Imaginary part of wavenumbers and the corresponding starting current values obtained from PIC simulations [3] as a function of the groove height h (squares, groove width w fixed at 60 μm) as well as groove width w (rounds, groove height h fixed at 100 μm). The other parameters are given in Table I.

modulation of the electrons. Coherent SPR is achieved only when the modulation of the electrons is sufficiently strong to induce density modulation, i.e., electron bunching, in order to build up wave oscillation in the structure. This occurs when the dc electron beam current exceeds a certain threshold value, which is defined as the starting current [3], [5], [24]. It is thus essential to understand how this starting current depends on the circuit parameters.

The SPR growth rate is expected to be correlated with the starting current of coherent SPR. The starting current is expected to be lower for gratings with a higher spatial growth rate. Thus, at those grating parameters with a maximum growth rate, we expect a minimum starting current.

In Fig. 6, we compare the spatial growth rate in Fig. 5(b) with the starting currents from PIC simulations in [3]. In the PIC simulation, 35 periods of grating were used, and all the other parameters remain as in Table I. Note that, for simplicity, we did not consider losses in either the theoretical calculation or the PIC simulation. It can be seen that the pattern of $\bar{k}_i$ follows very closely that of the starting current. Note the linear and log scale used to plot the $-\bar{k}_i$ and the starting current, respectively, which precisely confirms that the exponential wave growth $e^{-k_i x}$ follows the scaling of the starting current as a function of w and h. Note also that in our calculation here, the boundary conditions at the two ends of the interacting grating are not considered, which is in contrast to the traditional method for BWO analysis based on Johnson's approach, where the boundary conditions are critical [24].

The physical reason for the strong correlation between the spatial growth rate and the start current may be understood as follows. It is well known that in [3], [25], [26], for coherent radiation, the radiation power P scales as the square of the number of electrons per bunch N or, equivalently, the square of beam current I as

$$P \propto E^2 \propto N^2 \propto I^2 \tag{4}$$

where E is the electric field of the radiation. During the beam–structure interaction, the radiation is amplified when it travels from one end to another, through a spatial growth factor $e^{|k_i|L_G}$, where L_G is the total length of the interacting grating. The resulting radiation field is proportional to the spatial growth rate

$$E \propto e^{|k_i|L_G}. \tag{5}$$

Therefore, it can be seen from the above two scalings that the spatial growth rate is directly proportional to the beam current

$$e^{|k_i|L_G} \propto I. \tag{6}$$

We also calculated $-\bar{k}_i$ for different beam currents, all showing the same pattern as in Fig. 6, which confirms the robustness of calculating only the spatial growth rate to infer the scaling of the starting current for different circuit parameters.

Finally, we would like to note that the 2-D current density listed in Table I and Fig. 6 would yield a current on the order of milliamperes if one considers a practical field emitter with a transverse dimension of micrometer scale, which may be realized by carbon-nanotube fiber (CNF)-based field emitters as recently demonstrated experimentally [27], [28], [29]. For real device design, 3-D models with the requirement of electron beam properties [30] need to be constructed.

V. Conclusion

In summary, we analyze the SPR operation frequency and growth rate using the cold- and hot-tube dispersion relations. We systematically show how the operating frequencies of SPR have changed with different grating parameters using cold-tube dispersion relations where the grating period has been fixed. We demonstrate that the spatial growth rate of SPR calculated from the hot-tube dispersion relation has the same scaling dependence on the grating parameters as the starting current calculated from PIC simulations. Thus, we confirm that the grow rate calculation using the hot-tube dispersion relation can be used to predict the optimal grating parameters to minimize the starting current of SPR. This approach has a significantly reduced computational cost compared to either direct PIC simulations or the traditional Johnson's approach using the BWO condition of zero-drive instability [24]. As both the operation frequency of SPR and its growth rate depend strongly on the grating parameters, both the cold- and hot-tube dispersion relations can be used in combination to minimize the starting current at the desired radiation frequency. While we apply our analysis to the effects of grating parameters on SPR, we expect that our dispersion relation treatment to grating optimization is applicable to study linear free-electron beam-based vacuum devices in general and in various geometries (e.g., cylindrical geometry).

References

[1] S. J. Smith and E. M. Purcell, "Visible light from localized surface charges moving across a grating," *Phys. Rev.*, vol. 92, p. 1069, Nov. 1953, doi: 10.1103/PhysRev.92.1069.

[2] F. S. Rusin and G. D. Bogomolov, "Orotron—An electronic oscillator with an open resonator and reflecting grating," *Proc. IEEE*, vol. 57, no. 4, pp. 720–722, Apr. 1969, doi: 10.1109/PROC.1969.7049.

[3] P. Zhang, L. K. Ang, and A. Gover, "Enhancement of coherent Smith–Purcell radiation at terahertz frequency by optimized grating, prebunched beams, and open cavity," *Phys. Rev. Special Topics-Accel. Beams*, vol. 18, no. 2, Feb. 2015, Art. no. 020702, doi: 10.1103/PhysRevSTAB.18.020702.

[4] V. Kumar and K.-J. Kim, "Optimization of parameters of Smith–Purcell BWO," in *Proc. FEL BESSY Berl. Ger.*, 2006, p. 69.

[5] V. Kumar and K.-J. Kim, "Analysis of Smith–Purcell free-electron lasers," *Phys. Rev. E, Stat. Phys. Plasmas Fluids Relat. Interdiscip. Top.*, vol. 73, no. 2, Feb. 2006, Art. no. 026501, doi: 10.1103/PhysRevE.73.026501.

[6] H. P. Freund and T. M. Abu-Elfadl, "Linearized field theory of a Smith–Purcell traveling wave tube," *IEEE Trans. Plasma Sci.*, vol. 32, no. 3, pp. 1015–1027, Jun. 2004, doi: 10.1109/TPS.2004.827612.

[7] P. Zhang, B. Hoff, Y. Y. Lau, D. M. French, and J. W. Luginsland, "Excitation of a slow wave structure," *Phys. Plasmas*, vol. 19, no. 12, Dec. 2012, Art. no. 123104, doi: 10.1063/1.4771678.

[8] Y. Y. Lau and D. Chernin, "A review of the ac space-charge effect in electron–circuit interactions," *Phys. Fluids B: Plasma Phys.*, vol. 4, no. 11, pp. 3473–3497, Nov. 1992, doi: 10.1063/1.860356.

[9] H. L. Andrews, C. H. Boulware, C. A. Brau, and J. D. Jarvis, "Dispersion and attenuation in a Smith–Purcell free electron laser," *Phys. Rev. Special Topics-Accel. Beams*, vol. 8, no. 5, May 2005, Art. no. 050703, doi: 10.1103/PhysRevSTAB.8.050703.

[10] D. Li *et al.*, "Growth rate and start current in Smith–Purcell free-electron lasers," *Appl. Phys. Lett.*, vol. 100, no. 19, May 2012, Art. no. 191101, doi: 10.1063/1.4711803.

[11] D. Li *et al.*, "Improve growth rate of Smith–Purcell free-electron laser by Bragg reflector," *Appl. Phys. Lett.*, vol. 98, no. 21, May 2011, Art. no. 211503, doi: 10.1063/1.3594243.

[12] W. Liu and Z. Xu, "Special Smith–Purcell radiation from an open resonator array," *New J. Phys.*, vol. 16, no. 7, Jul. 2014, Art. no. 073006, doi: 10.1088/1367-2630/16/7/073006.

[13] A. Tavousi, A. Rostami, G. Rostami, and M. Dolatyari, "3-D numerical analysis of Smith–Purcell-based terahertz wave radiation excited by effective surface plasmon," *J. Lightw. Technol.*, vol. 33, no. 22, pp. 4640–4647, Nov. 15, 2015.

[14] P. Rattanawan *et al.*, "An alternative technique for verification of terahertz Smith–Purcell radiation," *J. Phys. D, Appl. Phys.*, vol. 54, no. 47, Sep. 2021, Art. no. 475106, doi: 10.1088/1361-6463/ac2332.

[15] *Free-Electron Driven Terahertz Wave Sources Based on Simth–Purcell Effect | IntechOpen*. Accessed: May 27, 2022. [Online]. Available: https://www.intechopen.com/chapters/78629

[16] W. Liu, W. Li, Z. He, and Q. Jia, "Theory of the special Smith–Purcell radiation from a rectangular grating," *AIP Adv.*, vol. 5, no. 12, Dec. 2015, Art. no. 127135, doi: 10.1063/1.4939538.

[17] M. Cao, W. Liu, Y. Wang, and K. Li, "Dispersion characteristics of planar grating with arbitrary grooves for terahertz Smith–Purcell radiation," *Phys. Plasmas*, vol. 22, no. 3, Mar. 2015, Art. no. 033103, doi: 10.1063/1.4913577.

[18] A. Szczepkowicz, L. Schüchter, and R. J. England, "Frequency-domain calculation of Smith–Purcell radiation for metallic and dielectric gratings," *Appl. Opt.*, vol. 59, no. 35, pp. 11146–11155, Dec. 2020, doi: 10.1364/AO.409585.

[19] S. C. Yurt, A. Elfrgani, M. I. Fuks, K. Ilyenko, and E. Schamiloglu, "Similarity of properties of metamaterial slow-wave structures and metallic periodic structures," *IEEE Trans. Plasma Sci.*, vol. 44, no. 8, pp. 1280–1286, Aug. 2016, doi: 10.1109/TPS.2016.2535305.

[20] P. Wong, P. Zhang, and J. Luginsland, "Recent theory of traveling-wave tubes: A tutorial-review," *Plasma Res. Exp.*, vol. 2, no. 2, Jun. 2020, Art. no. 023001, doi: 10.1088/2516-1067/ab9730.

[21] D. Simon *et al.*, "On the evaluation of pierce parameters C and Q in a traveling wave tube," *Phys. Plasmas*, vol. 24, no. 3, 2017, Art. no. 033114, doi: 10.1063/1.4978474.

[22] C. F. Dong *et al.*, "Harmonic content in the beam current in a traveling-wave tube," *IEEE Trans. Electron Devices*, vol. 62, no. 12, pp. 4285–4292, Dec. 2015, doi: 10.1109/TED.2015.2490584.

[23] D. M. H. Hung *et al.*, "Absolute instability near the band edge of traveling-wave amplifiers," *Phys. Rev. Lett.*, vol. 115, no. 12, Sep. 2015, Art. no. 124801, doi: 10.1103/PhysRevLett.115.124801.

[24] H. R. Johnson, "Backward-wave oscillators," *Proc. IRE*, vol. 43, no. 6, pp. 684–697, Jun. 1955, doi: 10.1109/JRPROC.1955.278054.

[25] A. Gover, "Superradiant and stimulated-superradiant emission in prebunched electron-beam radiators. I. formulation," *Phys. Rev. Special Topics-Accel. Beams*, vol. 8, no. 3, Mar. 2005, Art. no. 030701, doi: 10.1103/PhysRevSTAB.8.030701.

[26] S. E. Korbly, A. S. Kesar, J. R. Sirigiri, and R. J. Temkin, "Observation of frequency-locked coherent terahertz Smith–Purcell radiation," *Phys. Rev. Lett.*, vol. 94, no. 5, Feb. 2005, Art. no. 054803, doi: 10.1103/PhysRevLett.94.054803.

[27] P. Zhang, S. B. Fairchild, T. C. Back, and Y. Luo, "Field emission from carbon nanotube fibers in varying anode-cathode gap with the consideration of contact resistance," *AIP Adv.*, vol. 7, no. 12, Dec. 2017, Art. no. 125203, doi: 10.1063/1.5008995.

[28] P. Zhang *et al.*, "Temperature comparison of looped and vertical carbon nanotube fibers during field emission," *Appl. Sci.*, vol. 8, no. 7, p. 1175, Jul. 2018, doi: 10.3390/app8071175.

[29] S. B. Fairchild *et al.*, "Carbon nanotube fiber field emission array cathodes," *IEEE Trans. Plasma Sci.*, vol. 47, no. 5, pp. 2032–2038, May 2019, doi: 10.1109/TPS.2019.2900219.

[30] K.-J. Kim and V. Kumar, "Electron beam requirements for a three-dimensional Smith–Purcell backward-wave oscillator for intense terahertz radiation," *Phys. Rev. Special Topics-Accel. Beams*, vol. 10, no. 8, Aug. 2007, Art. no. 080702, doi: 10.1103/PhysRevSTAB.10.080702.